In vivo magnetomotive optical molecular imaging using targeted magnetic nanoprobes

Renu John[a], Robabeh Rezaeipoor[a], Steven G. Adie[a], Eric J. Chaney[a], Amy L. Oldenburg[a], Marina Marjanovic[a], Justin P. Haldar[a], Bradley P. Sutton[a,b], and Stephen A. Boppart[a,b,c,1]

[a]Beckman Institute for Advanced Science and Technology, [b]Department of Bioengineering, and [c]Departments of Electrical and Computer Engineering, and Medicine, University of Illinois at Urbana-Champaign, Urbana, IL 61801

Edited by Erich P. Ippen, Massachusetts Institute of Technology, Cambridge, MA, and approved February 26, 2010 (received for review December 1, 2009)

Dynamic magnetomotion of magnetic nanoparticles (MNPs) detected with magnetomotive optical coherence tomography (MM-OCT) represents a new methodology for contrast enhancement and therapeutic interventions in molecular imaging. In this study, we demonstrate in vivo imaging of dynamic functionalized iron oxide MNPs using MM-OCT in a preclinical mammary tumor model. Using targeted MNPs, in vivo MM-OCT images exhibit strong magnetomotive signals in mammary tumor, and no significant signals were measured from tumors of rats injected with nontargeted MNPs or saline. The results of in vivo MM-OCT are validated by MRI, ex vivo MM-OCT, Prussian blue staining of histological sections, and immunohistochemical analysis of excised tumors and internal organs. The MNPs are antibody functionalized to target the human epidermal growth factor receptor 2 (*HER2 neu*) protein. Fc-directed conjugation of the antibody to the MNPs aids in reducing uptake by macrophages in the reticulo-endothelial system, thereby increasing the circulation time in the blood. These engineered magnetic nanoprobes have multifunctional capabilities enabling them to be used as dynamic contrast agents in MM-OCT and MRI.

cancer | targeting | multimodal imaging | optical imaging

Recent advances in the synthesis and functionalization of molecular imaging nanoprobes have enabled biomedical imaging of malignancies in the body with high specificity and spatial localization. Biomedical imaging modalities such as fluorescence imaging (1), MRI (2), ultrasound imaging (3), photo-acoustic imaging (4), PET (5), and optical coherence tomography (OCT) (6) are being used to image nanoprobes and address the challenges involved in noninvasive in vivo imaging of biological tissues. Optical coherence tomography (7) is an emerging clinical imaging technology that is capable of mapping three-dimensional structural information of biological tissues based on their optical scattering properties with spatial resolutions comparable to histology. With advances in the development of catheters and endoscopes for clinical applications, OCT has also evolved as a promising noninvasive or minimally invasive diagnostic tool for imaging internal organs (8).

A variety of imaging modalities, including OCT, employ molecular imaging probes as passive contrast agents (6) that are inherently static in nature. Magnetomotive optical coherence tomography (MM-OCT) is a method for imaging a distribution of magnetic molecular imaging agents in biological specimens (9–11). Most optical imaging modalities rely on the inherent static properties of molecular agents such as fluorescence, bioluminescence, scattering differences, absorption, or polarization for achieving molecular contrast. Dynamic contrast enhancement in OCT through transient absorption changes induced by a pump beam in a pump-probe OCT system (12) and through dynamic temperature modulations in a photothermal OCT system (13, 14) have been reported as alternate methods of achieving contrast. MM-OCT is a technique that exploits dynamic magnetomotive-induced contrast in imaging. The dynamic nature of nanoprobes that are actuated externally using a magnetic field makes MM-OCT unique in its implementation and capable of detecting ultralow concentrations of magnetic nanoparticles (MNPs) with a sensitivity of 2 nM (27 μg/g of MNPs in phantoms and biological tissues) using a magnetic field as low as 0.08 T (11). MRI typically has detection thresholds in the range of a few hundreds of iron oxide nanoparticle-labeled cells in tissues (15). Because the dynamic magnetomotion of the MNPs results in physical nanometer-scale displacements within tissues, these molecular agents can also effectively be exploited to probe the biomechanical properties of the tissues (16).

The role of molecular agents such as quantum dots (17), gold nanoshells (18), carbon nanotubes (19), gold nanoparticles (20), gadolinium nanoparticles (21), superparamagnetic iron oxide nanoparticles (2, 22), polymeric nanoparticles (23), and microspheres (24) to enhance imaging and diagnostic capabilities is well established (6). Superparamagnetic iron oxide MNPs are promising molecular-specific imaging agents for MM-OCT owing to their versatile properties such as ease of fabrication, formation of hydrophilic suspensions with high biocompatibility, coating with a wide variety of natural and synthetic polymer materials (25, 26), and functionalization with a number of targeting agents including antibodies (27, 28), polypeptides, and oligonucleotides (26). Target-specific MNPs also find applications in therapy involving site-specific drug delivery, and hyperthermia (29, 30). The superparamagnetic nature and property of these MNPs to shorten T2* relaxation times in MRI enable the use of iron oxide MNPs as unique contrast agents for multimodal imaging applications that involve magnetomotion, dynamic contrast enhancement, and nuclear magnetic resonance.

In this study, we demonstrate in vivo MM-OCT imaging of dynamic functionalized MNPs in a preclinical mammary tumor model. The results of in vivo MM-OCT are validated by MRI, ex vivo MM-OCT, Prussian blue staining of histological sections, and immunohistochemical analysis of excised tumors and internal organs. We describe the synthesis of engineered, functionalized, biocompatible MNPs with appropriate size and coating to have good tolerances and long circulation times, as is well known in preclinical studies (19, 23, 26). These MNPs are antibody functionalized to target the human epidermal growth factor receptor 2 (*HER2 neu*) protein (27, 28), which is overexpressed in about 30% of invasive human breast carcinomas (31, 32). This study demonstrates the feasibility of multimodal imaging using MNPs as dynamic contrast agents for in vivo tumor imaging using MM-OCT and MRI. These magnetic nanoprobes can also be incorporated into systems that require magnetic manipulation of nanoprobes, including magnetic field-guided drug delivery systems for cancer treatment.

Author contributions: S.A.B. designed research; R.J., R.R., S.G.A., E.J.C., M.M., and J.P.H. performed research; R.J., R.R., S.G.A., A.L.O., and B.P.S. contributed new reagents/analytic tools; R.J., S.G.A., E.J.C., B.P.S., and S.A.B. analyzed data; and R.J. wrote the paper.

The authors declare no conflict of interest.

This article is a PNAS Direct Submission.

[1]To whom correspondence should be addressed. E-mail: boppart@illinois.edu.

This article contains supporting information online at www.pnas.org/cgi/content/full/0913679107/DCSupplemental.

MNPs act as dynamic contrast agents when mechanically actuated by an externally applied alternating magnetic field and subsequently modulate the optical scattering properties of the local tissue microenvironment under observation. The deformations and displacements in the local tissue microenvironment due to magnetomotion can effectively be detected by an ultrasensitive phase-resolved OCT system (11, 33) with a displacement sensitivity of a few tens of nanometers. In the MM-OCT system (Fig. 1), the magnetic field is applied using a ring-shaped custom-designed air-core solenoid with water cooling (Fig. 1*C*), and in vivo imaging is performed on the specimen placed directly below the solenoid bore. Within the imaging volume of the specimen, the radial components of the magnetic field are negligible and the magnetic field gradient is predominantly in the axial direction. The 20–30-nm diameter MNPs [transmission electron microscopy (TEM) shown in Fig. 1*B*] undergo magnetomotion due to the magnetic field gradient, resulting in dynamic nanoscale displacements of the local tissue microenvironment, and shift the amplitude and phase of the interference pattern detected by the OCT system. The magnetomotive response of MNPs in a gel-based tissue phantom to different magnetic field excitations can be demonstrated by performing M-mode imaging (Fig. 1*D*).

MM-OCT imaging is performed using a sinusoidal magnetic field excitation with a frequency matched to the mechanical resonance of the biological specimen to optimize imaging sensitivity and contrast. This resonant mechanical frequency, which is a key to the viscoelastic biomechanical properties of the tissue (16), is measured prior to MM-OCT imaging by applying a step excitation or sweep of frequencies. Two-dimensional B-mode scanning of the specimen is performed twice, acquiring one image with the field off and one with the field modulated. Mechanical excitation of the MNPs is coupled to B-mode OCT scanning by modulating the magnetic field several cycles during the time required to mechanically scan the imaging beam spot over one resolution point. A Fourier transform of the spectral interference pattern after background subtraction of the reference field intensity subsequently yields the B-mode OCT image. The magnetomotive contrast signal is extracted from the Fourier transform of the 2D OCT data along the transverse-time direction by bandpass filtering about the magnetic modulation frequency (11).

Results and Discussions

Preliminary MM-OCT studies were performed on mammary tumor tissues soaked with 1 mg/mL of the MNP solution for 1 h to verify the magnetomotive properties of the MNPs (Fig. S1*A*). Studies have also shown that the MNPs exhibit strong negative T2* contrast in MRI (Fig. S1*B*). Appropriate time periods for circulation, concentrations of targeted MNPs, and their general biodistribution in the in vivo model were determined through preliminary experiments. Studies were also carried out on this N-methyl-N-nitrosourea (MNU) carcinogen-induced rat mammary tumor model to evaluate the time-dependent and tumor-size-dependent expression levels of the *HER2* receptor (Fig. S2), as we had done for the $\alpha_v\beta_3$ integrin in a related study (34). To our knowledge, this expression profiling had not been reported in the literature and was essential for targeting these MNPs in this well-known animal tumor model. In this study, 65 mammary tumors of different sizes [from a very early stage (<0.1 cm) to a late stage of growth (2.0 × 2.2 cm)] were collected from 36 rats at different time periods (up to six to eight weeks) after the administration of the MNU carcinogen. Dissected tumors were used for immunohistochemical analysis using a commercial anti-*HER2* antibody (Cat. # PC04, Calbiochem) and a fluorescein-labeled secondary antibody to quantify the expression profile of this tumor marker. Results showed that expression level more strongly correlated with tumor size rather than time postexposure. Quantitative analysis based on relative fluorescence intensity of tumor sections vs. tumor size showed a linear and 16-fold increase in expression level between tumors 0.25 cm and 1.40 cm in diameter (Fig. S2). In larger tumors (~2 cm diameter), we observed some down-regulation in the expression of this marker.

In vivo studies were carried out on a MNU carcinogen-induced rat mammary tumor model. In vivo MM-OCT images from tumors of targeted MNP-, nontargeted MNP-, and saline-injected rats (Fig. 2 *A* and *B*) clearly exhibit an accumulation of anti-*HER2*-conjugated MNPs only in the tumor of the rat injected with targeted MNPs. A bar chart representing mean

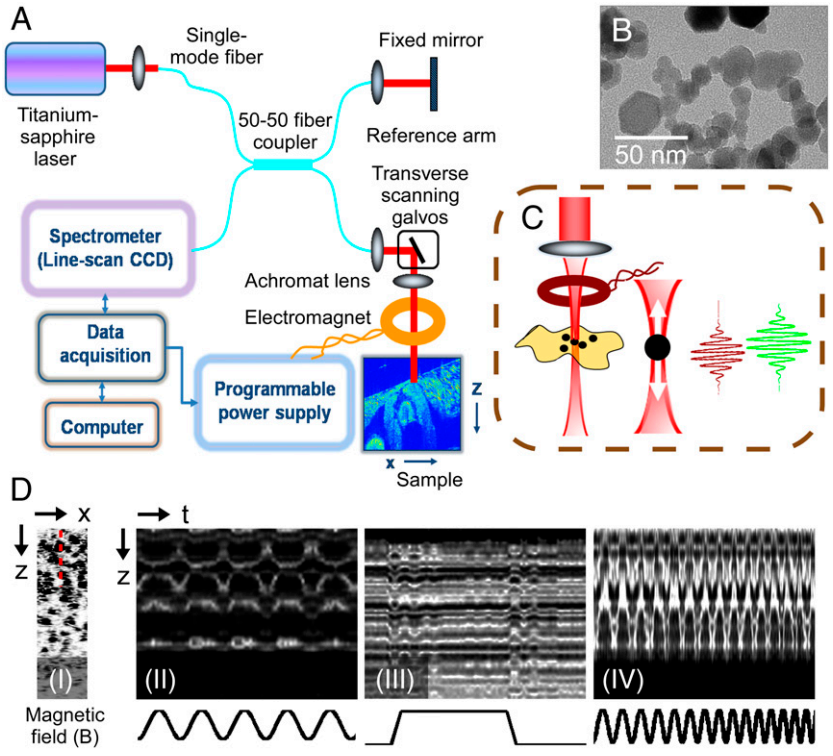

Fig. 1. MM-OCT principle. (*A*) Schematic of the experimental setup. (*B*) TEM of the MNPs used in the study. (*C*) Close-up of the sample arm with focusing lens, electromagnet, and specimen showing axial magnetomotive displacements of MNPs and corresponding change in the OCT interferogram. (*D*) (I) B-mode image through a MNP-silicone phantom. (II–IV) Representative zoomed-in images of M-mode scans along the dashed red line marked in (I) showing magnetomotion in the sample on application of a (II) sinusoidal, (III) pulse, and (IV) sweep of frequencies of the magnetic field.

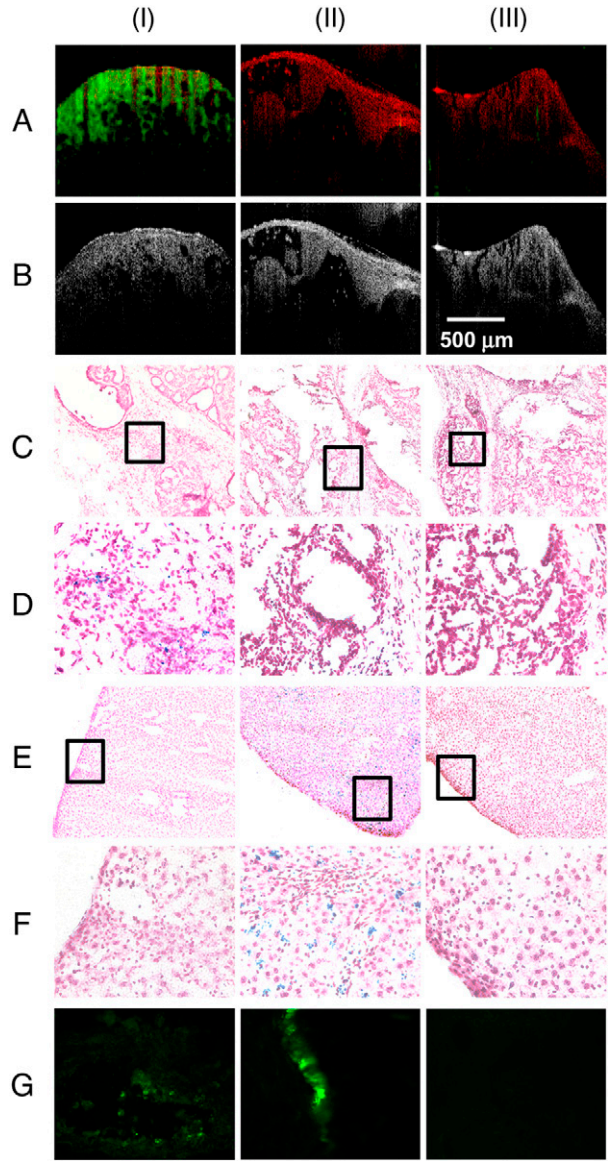

Fig. 2. In vivo (*A*) MM-OCT and (*B*) OCT images. MM-OCT signal (green channel) is superposed on the OCT signal (red channel). PB-stained sections of (*C*, *D*) tumors and (*E*, *F*) livers from (I) targeted MNP-injected, (II) nontargeted MNP-injected, and (III) saline-injected rats. PB-stained sections in *D* and *F*, at 40×) represent the boxed regions in *C* and *E*, at 10×, respectively. (*G*) Immunohistochemical-stained sections from (I) tumor from a targeted MNP-injected rat, (II) tail injection site from a targeted MNP-injected rat, and (III) tumor from a saline-injected rat.

MM-OCT signal values (in dB) from five B-mode images over a 2.5 mm × 2 mm area of each specimen are illustrated (Fig. 3), with the error bars representing the standard deviations. Each B-mode scan was 4,000 pixels in width by 1,024 pixels in depth. Statistical significance of the MM-OCT signal intensities was calculated on representative datasets from three rats using analysis of variance, and the p values are reported. There was a statistically significant MM-OCT signal intensity only from the tumor of the rat injected with anti-*HER2*-conjugated MNPs, in comparison to the MM-OCT signals from tumors from any of the rats injected with nontargeted MNPs or saline ($p < 0.0001$).

In vivo MM-OCT was followed by ex vivo MM-OCT imaging of internal organs and tumors from all animals. There were no significant MM-OCT signals from any of the internal organs of rats injected with targeted MNPs compared to the MM-OCT signals from excised tumors ($p < 0.0001$) (Fig. 3), with the exception of spleen, which is explained below. Comparison of MM-OCT signal strengths from the livers indicate there was a significant accumulation of MNPs in the livers of rats injected with nontargeted MNPs ($p < 0.0001$) and minimal accumulation in the livers of rats injected with targeted MNPs. This result supports the expected behavior of these MNPs with Fc-directed conjugation of antibodies, which reduces MNP trapping by the reticuloendothelial system and facilitates their circulation and transport to targeting sites (31). In all the cases, spleen exhibited a background MM-OCT signal because of its inherent paramagnetism from the presence of the iron protein ferritin, which is consistent with positive Prussian blue staining of the spleens. Hence, in rats injected with nontargeted MNPs, weak MM-OCT signals were obtained from the lungs and spleen showing weak nonpreferential accumulation of MNPs in these internal organs. In rats injected with saline, and after taking into account the false positive MM-OCT signal from spleen, there were no significant MM-OCT signals from any of the internal organs.

In vivo 3D MRI was performed immediately prior to and 6 h after injection of targeted MNPs, nontargeted MNPs, and saline to validate MM-OCT results. The large shift observed in the post-injection plot (Fig. 4*A*) toward smaller T2* values demonstrates negative T2* contrast, indicating accumulation of MNPs within the tumor of the rat injected with targeted MNPs. This is in contrast to the nontargeted and saline cases (Fig. 4 *B* and *C*), which either exhibit a minimal shift toward smaller T2* values or show a shift toward larger T2* values, respectively.

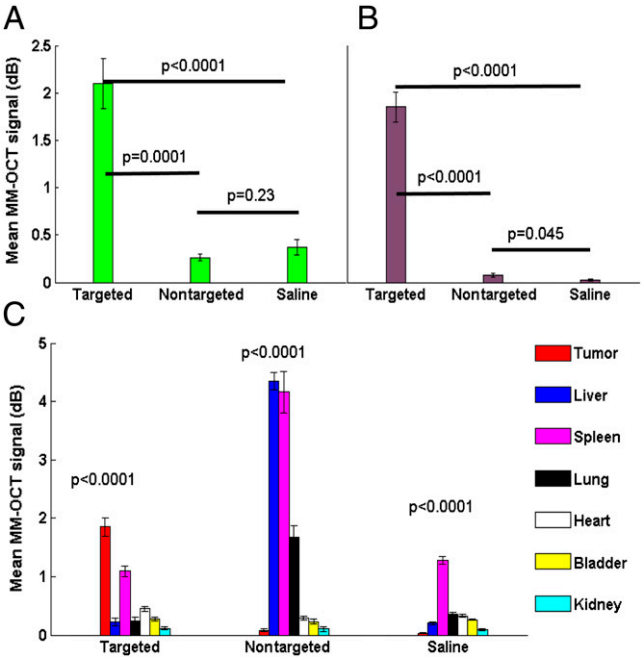

Fig. 3. MM-OCT signal intensities observed in vivo and ex vivo for the three cases in study. Comparison of (*A*) in vivo tumor data and (*B*) ex vivo tumor data for the three cases is shown. Statistical analysis based on analysis of variance indicate statistically significant MM-OCT signals from tumor of rat injected with targeted MNPs compared to tumor from rat injected with nontargeted MNPs or from rat injected with saline ($p = 0.0001$ and $p < 0.0001$, respectively). (*C*) Comparison of ex vivo MM-OCT signal data from tumors and internal organs for each case. For rats injected with targeted MNPs (*C Left*), statistical analysis shows a significant MM-OCT signal from tumor only, compared to the internal organs ($p < 0.0001$). For rats injected with nontargeted MNPs (*C Center*), MM-OCT signal strength is significantly higher in liver ($p < 0.0001$), and weak signals were obtained from lung and spleen. Note that elevated signals from spleen are recognized as falsely positive due to the presence of the iron protein ferritin. For rats injected with saline (*C Right*), there is only statistically significant MM-OCT signal from spleen ($p < 0.0001$) compared to the internal organs, due to the presence of ferritin.

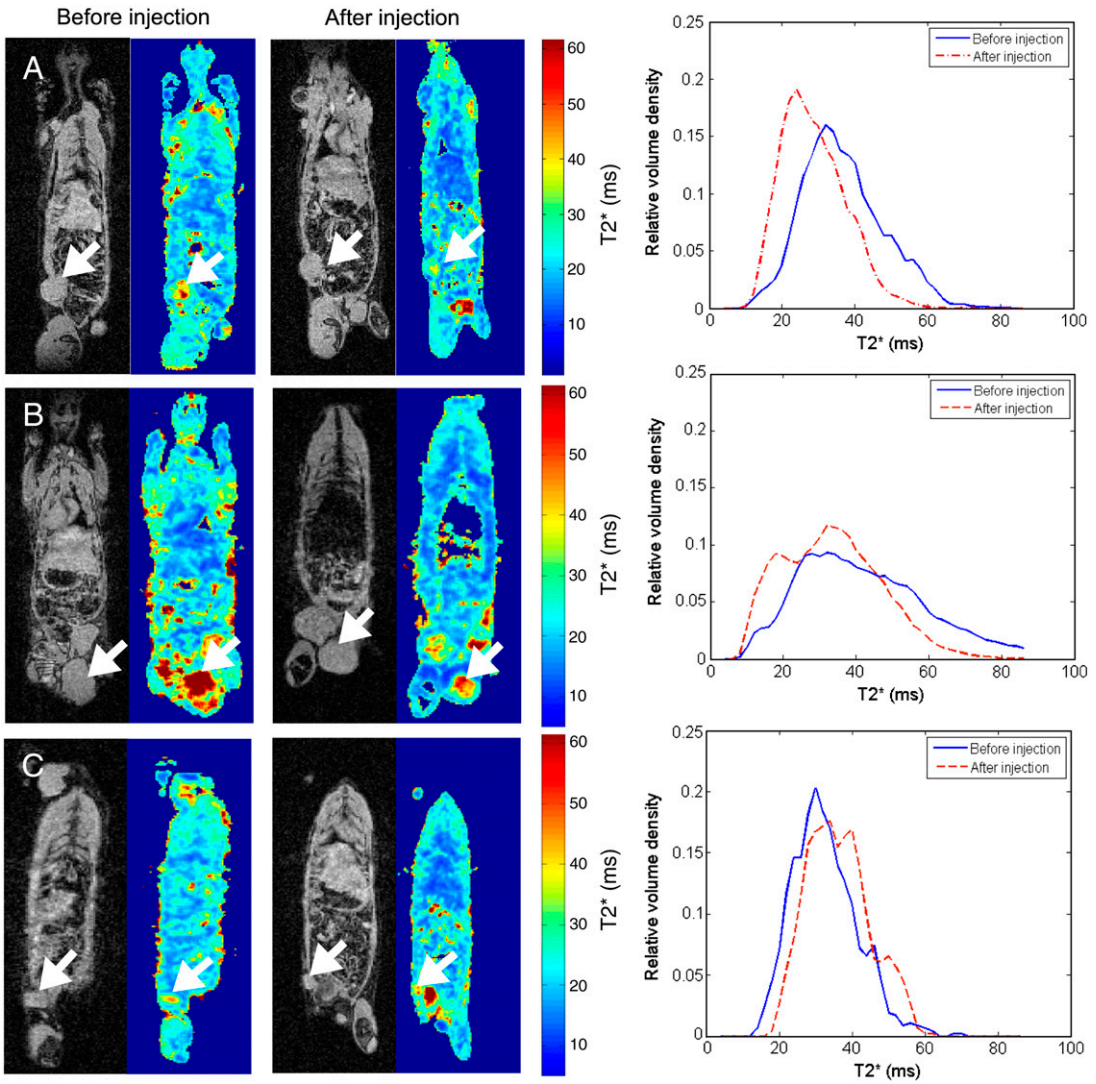

Fig. 4. Coronal slices from a 3D MRI dataset with corresponding T2* maps and plots of T2* values before injection and 6 h postinjection from (*A*) rat injected with targeted MNPs, (*B*) rat injected with nontargeted MNPs, and (*C*) rat injected with saline. Plots (right column) represent T2* values present within the segmented 3D volume of the corresponding tumors noted by the arrows.

Prussian blue (PB) staining performed on histological sections of tumors from targeted MNP-injected rats showed the presence of MNPs, and all of the tumors from rats injected with nontargeted MNPs or saline were PB negative (Fig. 2 *C* and *D*). All internal organs from rats injected with targeted MNPs were PB negative. PB staining of liver sections from rats injected with nontargeted MNPs showed high accumulation of MNPs (Fig. 2 *E* and *F*), while liver sections from all other cases were negative. The PB-stained histological sections of lungs, spleen, and urinary bladder from rats injected with nontargeted MNPs showed very weak traces of MNPs. The results of PB staining for spleens from targeted MNP-, nontargeted MNP-, and saline-injected animals showed strong false positives as expected. Analysis of immunohistochemically stained cryosections from a representative tumor from a rat injected with targeted MNPs (Fig. 2*G*) confirmed the presence of anti-*HER2* conjugated MNPs. The results are referenced to positive control tissue dissected from the tail region at the site of injection, and negative control tumor tissue from a saline-injected rat.

In this study, we have demonstrated in vivo MM-OCT imaging of targeted MNPs in a preclinical mammary tumor model. Development of functional targeted nanoprobes for site-specific molecular imaging is one of the challenges in biomedical research. We have fabricated magnetic nanoprobes functionalized with anti-*HER2* antibody targeted to *HER2 neu* protein, which is overexpressed in mammary tumors. The in vivo and ex vivo MM-OCT results demonstrate that the targeted MNPs accumulated in the tumors. The results of in vivo MRI, and histological methods such as PB staining and immunohistochemical analysis, validate the use of MM-OCT as a sensitive imaging modality for detecting targeted molecular nanoprobes in tumors and support our experimental in vivo and ex vivo MM-OCT findings that most of the targeted MNPs accumulated preferentially in tumors, with few MNPs accumulating in the kidneys and urinary bladder. The nontargeted MNPs were widely distributed to organ systems with no preference to tumors, finally accumulating in the liver after 8 to 12 h post tail-vein injection. Site-specific accumulation of these nanoprobes is an important step toward treatment of various cancers using targeted drug delivery and hyperthermia effects. The Fc-directed conjugation of the antibody to the MNPs likely was responsible for significantly reducing the targeted MNP accumulation in the liver.

Studies have indicated that the expression levels of the *HER2* protein in various types of cancers vary depending on many factors such as size of tumor (Fig. S2) and stage of growth (29). Accumulation of MNPs at targeted sites, or efficiency of targeted delivery, ultimately depends on expression levels of the targeted receptor or antigen at the tumor site, and physiological conditions under which the agents are administered and circulated. This study found that this animal model tolerated the presence of targeted MNPs for 12 h, without premature death under anesthesia. Cytotoxicity and viability studies for these targeted and

nontargeted dextran-coated MNPs are under investigation using different cell lines and this preclinical model.

The negative T2* contrast observed in MRI images of tumors suggests the possibility of using these engineered MNPs for coregistered multimodal imaging with MRI and MM-OCT. Wide-field whole-body and organ-specific 3D MRI imaging with sub-millimeter resolution can be used to spatially guide micron-scale resolution MM-OCT imaging that would be performed over millimeter-scale fields of view. Clinically, MRI would be used to localize tumors, followed by MM-OCT for intraoperative-guided biopsy or surgery for the complete resection of the tumor. Intraoperative OCT has recently shown feasibility for identifying positive tumor margins during breast lumpectomy procedures (35), but could additionally benefit from site-specific molecular imaging and contrast enhancement of tumor cells. In this study, due to locations of imaging systems and animal transport, MM-OCT and MRI were performed at different time points after injection, which influenced the level of intermodality correlation that was observed in vivo. Temporal dynamics of MNP accumulation and clearance can be quantified with further MRI studies, which could also determine optimal time points for coregistered multimodal imaging with MRI and MM-OCT.

Ultimately, development of multimodal imaging platforms exploiting these multifunctional magnetic nanoprobes would likely play a significant role in the detection and diagnosis of various cancers, offering real-time tracking and visualization across a range of size scales (whole-body to cellular events) as well as the next generation of therapeutic strategies. New advances in catheter- and endoscope-based OCT technologies allow for the use of MM-OCT at internal sites accessed via minimally invasive procedures. This class of dynamic magnetomotive contrast agents offers the potential to expand our multimodal molecular imaging capabilities for the detection of cancer.

Materials and Methods

Preparation of targeted magnetic nanoparticles. Dextran-coated iron oxide magnetic nanoparticles (MNPs) were prepared by reaction of a mixture of ferric and ferrous ions with dextran polymers under alkaline condition (36–47). A mixed solution of ferrous and ferric ions in a molar ratio equal to 0.57 was prepared from 6.4% $FeCl_2 \cdot 4H_2O$ and 15.1% $FeCl_3 \cdot 6H_2O$ in deaerated, distilled water. An equal volume of a 20% (wt/vol) polymer solution in distilled water was then mixed with the iron solution and kept at a constant 60 °C for 15 min under nitrogen purging to avoid oxidation. An approximately equal volume of 7.5% (vol/vol) aqueous ammonia solution was then added dropwise to the iron-polymer mixture to maintain the pH at 11.5 during heating at 60 °C for 15 min, with vigorous stirring. Unbound dextran was separated from MNPs by molecular sieve chromatography using a Sephadex G-300 column equilibrated with 0.01 M phosphate buffer at pH 7.4. After fractionation, the anthrone assay was used to determine the presence of any unbound dextran in the eluted fractions (42).

Fc-directed conjugation of the antibody molecules is made possible through reductive amination coupling between free amino groups in the Fc region of the antibody and reactive aldehyde groups (41, 42). To create reactive aldehyde groups on MNP surfaces, oxidation of dextran is carried out under mild conditions. A volume of 0.25 mL of 25 mmol/L $NaIO_4$ (final concentration 5 mmol/L) was used to oxidize 1 mL of Fe-Dex-MNPs. The reaction was kept away from light and oxygen and was constantly stirred (150 rpm). Next, 0.2 mL of 2 mol/L ethylene glycol was added and stirred for 30 min to terminate oxidation. Excess periodate was removed by dialyzing the suspension for 24 h against 0.01 mol/L PBS at 4 °C. Particle concentration was determined by dry weight analysis after oxidation of dextran-coated MNPs.

A total of 25 μg of rabbit polyclonal anti-*HER2* antibody (c-erbB-2/*HER-2/neu* Ab-1 (21n), Thermo Fisher Scientific, Cat. # RB-103PABX) per mg of MNPs was added to the particles and placed in the dark at 4 °C for 8 h. This primary antibody was found to have a known reactivity with *HER2* for this rat tumor model (45). This step was followed by reduction with 0.5 mol/L $NaBH_4$ for 30 min to stabilize the new configuration. Uncoupled antibody was separated from conjugated particles by gel filtration chromatography on a Sephacryl S 300 column. The Fc-directed specificity and targeting properties were tested and verified on different cell lines (31).

Animal model. Inbred Wistar-Furth female rats ($N = 6$, 32 days old) (Jackson Labs) were used in this study. Experiments were performed in compliance with an experimental protocol approved by the institutional animal care and use committee at the University of Illinois at Urbana-Champaign. Rats were individually housed, fed standard rat chow pellets, and provided water and food ad libitum. Rats were kept on a 12-h light-dark cycle and housed in the biological resources facility at the Beckman Institute for Advanced Science and Technology at the University of Illinois at Urbana-Champaign. For mammary tumor induction, the carcinogen N-methyl-N-nitrosourea (MNU) (50 mg/kg body weight) was injected i.p. twice, at a one-week interval. The first injection was made in the left side and the second injection in the right side of the peritoneum. For a negative control, a group of three Wistar-Furth rats was kept under the same housing conditions and received injections of only the carrier buffer (0.9% NaCl, pH 4.0). Following MNU or saline control injections, animals were palpated weekly to determine mammary tumor development. From the six tumor-bearing rats, two rats each were injected with targeted MNPs, non-targeted MNPs, and saline. An MNP solution with a concentration of 30 mg/mL (5 mL/kg body weight) was administered intravenously to rats through the tail vein. MRI was performed immediately before and 6 h post injection on the rats. MM-OCT was performed after 10 h of injection. After anesthetizing the animals, they were placed supine on the MM-OCT platform and the mammary tumors were surgically exposed for in vivo MM-OCT imaging. The ex vivo MM-OCT studies, PB staining, and immunohistochemical analysis were performed on tumors and organs after removal from euthanized animals.

MM-OCT system. A spectral-domain OCT system with a $Ti:Al_2O_3$ femtosecond laser (KMLabs, Inc.) producing 800-nm light with a bandwidth of 120 nm (providing ~3-μm axial resolution in tissue) was used for these studies. The femtosecond laser was pumped by a frequency-doubled $Nd:YVO_4$ laser (Coherent, Inc.) with 4.5 W of 532-nm light. A single-mode fiber interferometer divided the broad band source light into the sample arm and a stationary reference arm. The sample-arm beam with a power of 10 mW was steered using galvanometer-mounted mirrors placed one focal length above a 30-mm achromatic imaging lens (providing ~12-μm transverse resolution). A water-cooled electromagnet driven by a 250-W power supply was used to achieve a magnetic field of ~0.08 T and a gradient of ~15 T/m within the sample imaging volume. The light beam on the specimen was scanned through the central bore of the solenoid. Interference between the reference and sample beams was measured with a custom-designed spectrometer composed of a grating, imaging lens, and line camera (Piranha 2, Dalsa Inc.) providing an optical imaging depth of 2 mm and line acquisition rates up to 33 kHz. The magnetic modulation frequency f_B was chosen to be between 56 Hz and 100 Hz for different tissue types based on previous studies that determined the optimal MM-OCT response achieved from these tissue specimens, which depended on their elastic modulus (47). A lower axial scan rate of 1 kHz was chosen to avoid excessive oversampling. The camera exposure time was 250 μs. Each B-mode scan was performed over 2.5 mm of the specimen (4,000 pixels in width by 1,024 pixels in depth) taking an acquisition time of 4 s. 3D sampling of the specimens was carried out with 0.5-mm spacing in the *y* direction, and each image was acquired twice, once with the modulating magnetic field on and once with the field off.

MRI studies. Three-dimensional in vivo MRI was performed with a 3T Siemens Magnetom Allegra MR Scanner imaging system using a high-performance gradient system (maximum gradient strength 40 mT/m) and a custom-built transmit/receive rf coil with an internal diameter of 8.0 cm. The rf coil was designed to meet the matching/tuning requirements of the Allegra MR Scanner. A coil-to-console interface (Clinical MR Solutions, LLC product) and custom software were employed. Imaging was conducted with a custom-designed T2*-weighted gradient echo multislice pulse sequence that enabled the effective capture of four echo times simultaneously at ~4, 10, 16, and 25 ms. Volumetric analysis of T2* was performed in Matlab to minimize potential sampling errors resulting from spatial T2* inhomogeneities observed in the 3D dataset that are attributable to natural T2* variations within tumors, and inhomogeneous distributions of MNPs within tumors. Three-dimensional T2* maps were calculated from 3D MRI datasets using least-squares linear regression applied to the natural logarithm of the time-resolved gradient echo signal. Segmentation of tumors was performed manually on a slice-by-slice basis.

Sampling and tissue sectioning. Rats were euthanized by CO_2 inhalation, followed by resection of tumors, liver, lungs, kidneys, bladder, heart, and spleen. Collected samples were placed in a freezing box containing isopropanol to control the rate of temperature decline and left at −80 °C overnight.

Subsequently, the samples were transferred into liquid nitrogen for long-term preservation. Frozen tissues were cryosectioned, with a thickness of 10 μm, using a cryostat (Leica CM 3050 S). Thin cryosections were overlayed on poly-L-lysine precoated slides (Histology Control Systems, Inc.), dried at room temperature for 30 min, and fixed with cold acetone for 15 min at 4 °C. For longer preservation, the fixed sections were kept at −80 °C before usage.

Prussian blue staining. Ten-micron-thick cryosections of specimens were washed with deionized water and placed in working iron stain solution (Sigma-Aldrich, HT20) for 10 min. After rinsing in deionized water, sections were counterstained in working pararosaniline solution for 5 min and rinsed in deionized water. After air drying, sections were mounted, covered by coverslips, and viewed with a light microscope. The working iron stain solution was freshly prepared by mixing equal volumes of potassium ferrocyanide solution and hydrochloric acid solution (Sigma-Aldrich). The working pararosaniline solution was prepared by adding 1 mL of pararosanilline solution (Sigma-Aldrich) to 50 mL of water.

Immunohistochemical analysis. For immunohistochemical analysis, fluorescein-5-isothiocyanate (FITC-isomer 1) conjugated to donkey anti-rabbit IgG (H + L) with minimal cross-reaction to rat was used as a secondary antibody (Lot No. 75970, Code No. 711-095-152, Jackson ImmunoResearch Laboratories, Inc.). First, fixed cryosections were washed 3× using PBS. All sections were pre-blocked with 10% normal donkey serum (in PBS + 1% BSA) for 30 min at room temperature in a humid box. After blocking, sections were washed 3 × 2 min using a washing buffer (PBS + 0.1% Tween 20). After washing, fluorescein-conjugated secondary antibody (1/100 dilution) was added to each section, incubated for 60 min in the humid box, then washed 3 × 2 min using a washing buffer. A drop of a hard set mounting medium (Vectashield, Vector Laboratories, Inc.) (H-1400) was used for each fluoro-immunostained section, which was then covered with a coverslip and kept at 4 °C for subsequent studies using fluorescence microscopy (Axiovert 200, Carl Zeiss, Germany).

ACKNOWLEDGMENTS. We thank Boris Odintsov from the Biomedical Imaging Center (BIC) at the Beckman Institute for Advanced Science and Technology, University of Illinois at Urbana-Champaign, for the fabrication of the rf coil for in vivo MRI studies, the research personnel at BIC for technical support, and Scott Robinson from the Imaging Technology Group at the Beckman Institute for Advanced Science and Technology for his assistance with TEM analysis. This research was supported in part by grants from the National Institutes of Health (Roadmap Initiative, NIBIB, R21 EB005321; NIBIB, R01 EB005221; NIBIB, R01 EB009073; and NCI RC1 CA147096, S.A.B.).

1. Graves EE, Weissleder R, Ntziachristos V (2004) Fluorescence molecular imaging of small animal tumor models. *Curr Mol Med* 4:419–430.
2. Bulte JWM, Kraitchman DL (2004) Iron oxide MR contrast agents for molecular and cellular imaging. *NMR Biomed* 17:484–494.
3. Liu J, et al. (2006) Nanoparticles as image enhancing agents for ultrasonography. *Phys Med Biol* 51:2179–2189.
4. Wang LV (2009) Multiscale photoacoustic microscopy and computed tomography. *Nat Photonics* 3:503–509.
5. Luker GD, Piwnica-Worms D (2001) Molecular imaging *in vivo* with PET and SPECT. *Acad Radiol* 8:4–14.
6. Boppart SA, Oldenburg AL, Xu C, Marks DL (2005) Optical probes and techniques for molecular contrast enhancement in coherence imaging. *J Biomed Opt* 10:041208.
7. Huang D, et al. (1991) Optical coherence tomography. *Science* 254:1178–1181.
8. Fujimoto JG, et al. (1995) Optical biopsy and imaging using optical coherence tomography. *Nat Med* 1:970–972.
9. Oldenburg AL, Gunther JR, Boppart SA (2005) Imaging magnetically labeled cells with magnetomotive optical coherence tomography. *Opt Lett* 30:747–749.
10. Oldenburg AL, Toublan FJ, Suslick KS, Wei A, Boppart SA (2005) Magnetomotive contrast for *in vivo* optical coherence tomography. *Opt Express* 13:6597–6614.
11. Oldenburg AL, Crecea V, Rinne SA, Boppart SA (2008) Phase-resolved magnetomotive OCT for imaging nanomolar concentrations of magnetic nanoparticles in tissues. *Opt Express* 16:11525–11539.
12. Rao KD, Choma M, Yazdanfar S, Rollins AM, Izatt JA (2003) Molecular contrast in optical coherence tomography using a pump-probe technique. *Opt Lett* 28:340–342.
13. Adler DC, Huang S-W, Huber R, Fujimoto JG (2008) Photothermal detection of gold nanoparticles using phase-sensitive optical coherence tomography. *Opt Express* 16:4376–4393.
14. Skala MC, Crow MJ, Wax A, Izatt JA (2008) Photothermal optical coherence tomography of epidermal growth factor receptor in live cells using immunotargeted gold nanospheres. *Nano Lett* 8:3461–3467.
15. Liu W, Frank JA (2009) Detection and quantification of magnetically labeled cells by cellular MRI. *Eur J Radiol* 70:258–264.
16. Crecea V, Oldenburg AL, Liang X, Ralston TS, Boppart SA (2009) Magnetomotive nanoparticle transducers for optical rheology of viscoeleastic materials. *Opt Express* 17:23114–23122.
17. Gao XH, et al. (2004) *In vivo* cancer targeting and imaging with semiconductor quantum dots. *Nat Biotechnol* 22:969–976.
18. Loo C, Lowery A, Halas N, West J, Drezek R (2005) Immunotargeted nanoshells for integrated cancer imaging and therapy. *Nano Lett* 5:709–711.
19. Shi Kam NW, O'Connell M, Wisdom JA, Dai H (2005) Carbon nanotubes as multifunctional biological transporters and near-infrared agents for selective cancer cell destruction. *Proc Natl Acad Sci USA* 102:11600–11605.
20. Sokolov K, et al. (2003) Real-time vital optical imaging of precancer using anti-epidermal growth factor receptor antibodies conjugated to gold nanoparticles. *Cancer Res* 63:1999–2004.
21. Sharma P, et al. (2007) Gd nanoparticulates: From magnetic resonance imaging to neutron capture therapy. *Adv Powder Technol* 18:663–698.
22. Lind K, Kresse M, Debus NP, Muller RH (2002) A novel formulation for superparamagnetic iron oxide particles enhancing MR lymphography: Comparison of physicochemical properties and the *in vivo* behaviour. *J Drug Target* 10:221–230.
23. Nasongkla N, et al. (2006) Multifunctional polymeric micelles as cancer-targeted, MRI-ultrasensitive drug delivery systems. *Nano Lett* 6:2427–2430.
24. Lee TM, et al. (2003) Engineered microsphere contrast agents for optical coherence tomography. *Opt Lett* 28:1546–1548.
25. Lee H, et al. (2006) Antibiofouling polymer-coated superparamagnetic iron oxide nanoparticles as potential magnetic resonance contrast agents for *in vivo* cancer imaging. *J Am Chem Soc* 128:7383–7389.
26. Gupta AK, Gupta M (2005) Synthesis and surface engineering of iron oxide nanoparticles for biomedical applications. *Biomaterials* 26:3995–4021.
27. Funovics MA, et al. (2004) MR imaging of the her2/neu and 9.2.27 tumor antigens using immunospecific contrast agents. *Magn Reson Imaging* 22:843–850.
28. Artemov D, Mori N, Ravi R, Bhujwalla ZM (2003) Magnetic resonance molecular imaging of the HER-2/*neu* receptor. *Cancer Res* 63:2723–2727.
29. McCarthy JR, Weissleder R (2008) Multifunctional magnetic nanoparticles for targeted imaging and therapy. *Adv Drug Deliver Rev* 60:1241–1251.
30. DeNardo SJ, et al. (2005) Development of tumor targeting bioprobes (in-chimeric L6 monoclonal antibody nanoparticles) for alternating magnetic field cancer therapy. *Clin Cancer Res* 11:7087s–7092s.
31. Rezaeipoor R, et al. (2009) Fc-directed antibody conjugation of magnetic nanoparticles for enhanced molecular targeting. *J Innov Opt Health Sciences* 2:387–396.
32. Camp RL, Dolled-Filhar M, King Bonnie L, Rimm DL (2003) Quantitative analysis of breast cancer tissue microarrays shows that both high and normal levels of HER2 expression are associated with poor outcome. *Cancer Res* 63:1445–1448.
33. Choma MA, Ellerbee AK, Yang C, Creazzo TL, Izatt JA (2005) Spectral domain phase microscopy. *Opt Lett* 30:1162–1164.
34. Rezaeipoor R, Chaney EJ, Oldenburg AL, Boppart SA (2009) Expression order of alpha-v and beta-3 integrin subunits in the N-methyl-N-nitrosourea-induced rat mammary tumor model. *Cancer Invest* 27:496–503.
35. Nguyen FT, et al. (2009) Intraoperative evaluation of breast tumor margins with optical coherence tomography. *Cancer Res* 69:8790–8796.
36. Duan H-L, Shen Z-Q, Wang X-W, Chao F-H, Li J-W (2005) Preparation of immunomagnetic iron-dextran nanoparticles and application in rapid isolation of *E.coli* 0157:H7 from foods. *World J Gastroentero* 11:3660–3664.
37. Shen T, Weissleder R, Papisov M, Bogdanov A, Brady TJ (1993) Monocrystalline iron oxide nanocompounds (MION): Physicochemical properties. *Magn Reson Med* 29:599–604.
38. Grüttner C, et al. (2007) Synthesis and antibody conjugation of magnetic nanoparticles with improved specific power absorption rates for alternating magnetic field cancer therapy. *J Magn Magn Mater* 311:181–186.
39. Tiefenauer LX, Kühne G, Andres RY (1993) Antibody-magnetite nanoparticles: *In vitro* characterization of a potential tumor-specific contrast agent for magnetic resonance imaging. *Bioconjugate Chem* 4:347–352.
40. Okon E, et al. (1994) Biodegradation of magnetite dextran nanoparticles in the rat: A histologic and biophysical study. *Lab Invest* 71:895–903.
41. Bonneaux F, Dellacherie E, Labrude P, Vigneron C (1996) Hemoglobin-dialdehyde dextran conjugates: Improvement of their oxygen-binding properties with anionic groups. *J Protein Chem* 15:461–465.
42. Wilson MB, Nakane PK (1976) The covalent coupling of proteins to periodate-oxidized sephadex: A new approach to immunoadsorbent preparation. *J Immunol Methods* 12:171–181.
43. Wang X, Yang L, Chen Z, Shin DM, (2008) Application of nanotechnology to cancer therapy and imaging. *CA-Cancer J Clin* 58:97–110.
44. Moghimi SM, Hunter AC, Murray JC (2005) Nanomedicine: Current status and future prospects. *FASEB J* 19:311–330.
45. Wang YXJ, Hussain SM, Krestin GP (2001) Superparamagnetic iron oxide contrast agents: Physicochemical characteristics and applications in MR imaging. *Eur Radiol* 11:2319–2331.
46. Gullick WJ, et al. (1987) Expression of the c-erbB-2 protein in normal and transformed cells. *Int J Cancer* 15:246–254.
47. John R, Chaney EJ, Boppart SA (6, 2009) Dynamics of magnetic nanoparticle-based contrast agents in tissues tracked using magnetomotive optical coherence tomography. *IEEE J Sel Top Quant Electron: Biophotonics* 10.1109/JSTQE.2009.2029547.

Supporting Information

John et al. 10.1073/pnas.0913679107

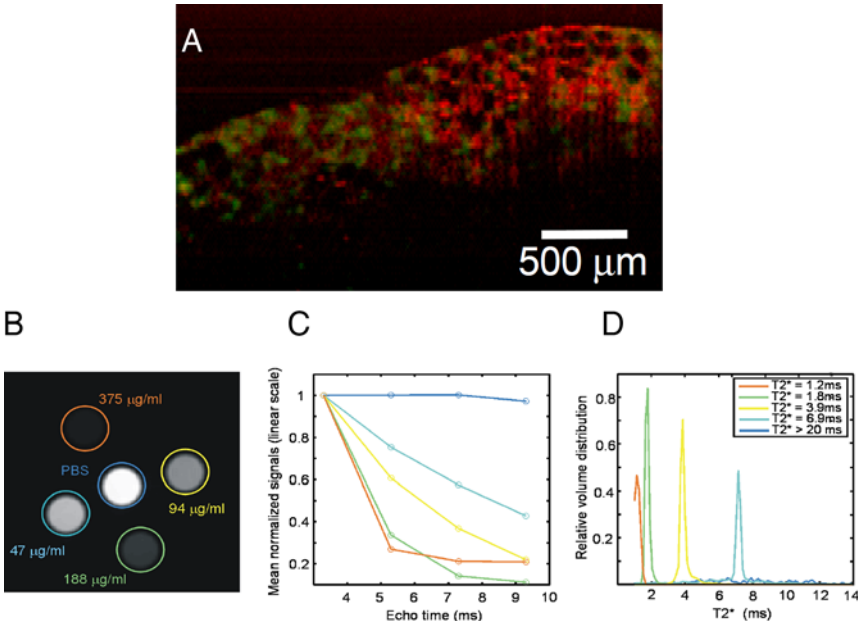

Fig. S1. (*A*) Magnetomotive optical coherence tomography (MM-OCT) image of a mammary tumor soaked in 1 mg/mL solution of dextran-coated MNPs for 1 h. MM-OCT signal (green channel) is superposed over the structural optical coherence tomography image (red channel). (*B*) A transverse slice from an MRI 3D dataset of vials containing different concentrations of MNPs in PBS solution. (*C*) Normalized signal decay curves vs. echo time. (*D*) Corresponding plot of T2* values present within the segmented 3D volumes marked in *B*. MRI was performed on a 14-T system. (Note that the decay curve for the pure PBS is too gradual to enable an accurate measurement for T2*.)

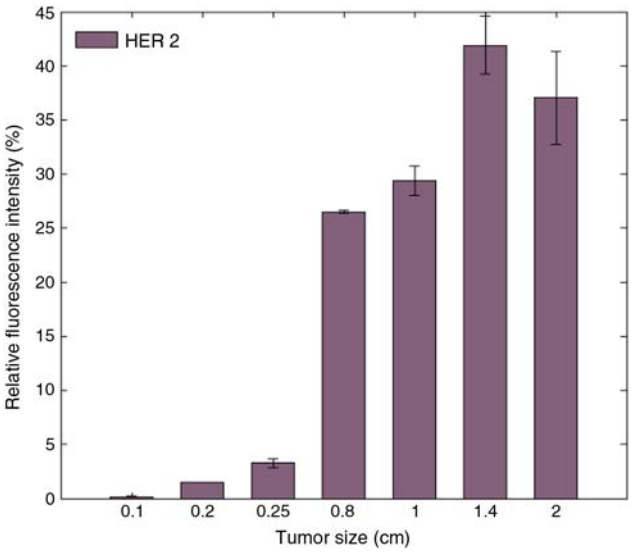

Fig. S2. Tumor marker expression levels in MNU-induced rat mammary tumor model. Quantitative analysis of relative fluorescence intensity from fluoro-immunostained tumor sections show *HER2* expression levels vs. tumor size. The error bars represent standard deviations from mean values.